








Cite this: *Nanoscale*, 2024, **16**, 299

The dual nature of biomimetic melanin†

Alexandra Mavridi-Printezi,  ‡^a Stefano Giordani,  ‡^a Arianna Menichetti,  ^{a,b}
 Dario Mordini,^a Andrea Zattoni,^a Barbara Roda,^a Lucia Ferrazzano,  ^a
 Pierluigi Reschiglian,^a Valentina Marassi*^a and Marco Montalti  *^{a,b}

Melanin-inspired nanomaterials offer unique photophysical, electronic and radical scavenging properties that are widely explored for health and environmental preservation, or energy conversion and storage. The incorporation of functional melanin building blocks in more complex nanostructures or surfaces is typically achieved *via* a bottom-up approach starting from a molecular precursor, in most cases dopamine. Here we demonstrate that indeed, the oxidative polymerization of dopamine, for the synthesis of melanin-like polydopamine (PDA), leads to the simultaneous formation of more than one nanosized species with different compositions, morphologies and properties. In particular, a low-density polymeric structure and dense nanoparticles (NP) are simultaneously formed. The two populations could be separated and analyzed in real time using a chromatographic technique free of any stationary phase (flow field fractionation, FFF). The results following the synthesis of melanin-like PDA showed that the NP are formed only during the first 6 hours as a result of a supramolecular self-assembly-driven polymerization, while the formation of the polymer continues for about 36 hours. The two populations were also separated and characterized using TEM, UV-vis absorption spectroscopy, fluorescence and light scattering spectroscopy, DLS, FTIR, ζ -potential measurements, gel electrophoresis and pH titrations. Interestingly, very different properties between the two populations were observed: in particular the polymer contains a higher number of catechol units (8 mmol g⁻¹ –OH) with respect to the NP (1 mmol g⁻¹ –OH) and presents a much higher antioxidant activity. The attenuation of light by NP is more efficient than that by the polymer especially in the Vis-NIR region. Moreover, while the NP scatter light with an efficiency up to 27% they are not fluorescent, and the polymer does not scatter light but shows an excitation wavelength-dependent fluorescence typical of multi-fluorophoric uncoupled systems.

Received 18th September 2023,
Accepted 17th November 2023

DOI: 10.1039/d3nr04696f

rsc.li/nanoscale

1. Introduction

Melanin-like materials, and in particular polydopamine (PDA), are finding outstanding applications in fields of high social and economic impact associated with human health,¹ energy conversion and accumulation, and environmental preservation.² The main reason for this success is that melanin-like nanomaterials combine an intrinsic biocompatibility with simplicity of preparation in their biomimetic forms, unique optical and electronic properties and unprecedented multifunctionality.

Although these unique features have been recognized and widely explored, these materials present a high complexity and a large variety of structures and morphologies, which are obscure up to now, making even their classification quite challenging.^{2b,3} In particular, even though PDA has found numerous applications in the form of films, water-soluble polymers and nanoparticles (NP), the relationship between the optical, chemical, physical and electronic properties of these materials and their chemical structure and morphology is still ignored to a large extent.^{2b} In fact, the main efforts of the scientific community have been mostly directed towards developing synthetic procedures able to lead to the main, but maybe not exclusive, formation of a specific form of PDA (*e.g.* NP rather than films). However, the actual presence of different PDA species in the same synthetic procedure was typically ignored, as well as the different mechanisms that lead to their formation. Here we demonstrate that in a typical preparative process, different forms of PDA are produced simultaneously, starting from the same molecular precursor dopamine (DA), and that they present very different properties. We

^aDepartment of Chemistry “Giacomo Ciamician”, Via Selmi 2, 40126 Bologna, Italy.
E-mail: valentina.marassi@unibo.it, marco.montalti2@unibo.it

^bTecnopolo di Rimini, Via Dario Campana, 71, 47922 Rimini, Italy

†Electronic supplementary information (ESI) available: Experimental details about synthesis and characterization. See DOI: <https://doi.org/10.1039/d3nr04696f>

‡These authors contributed equally.



also propose a chemical mechanism through which the different forms of PDA are produced, which, in particular, explains how the polymerization can lead either to poorly branched low-density polymeric species or to highly cross-linked materials as **NP**. Moreover, the important role of self-assembly in the formation of **NP** is underlined.⁴

In order to do this, two different strategies are combined. In the first approach, the formation of PDA starting from the molecular precursor DA in real time is followed by combining UV-vis absorption spectroscopy, dynamic light scattering (DLS) and field flow fractionation (FFF). FFF is a soft, size-based separation technique performed in the absence of a stationary phase thanks to the presence of a transversal field; when the field is in a perpendicular flow of solvent, the technique is named flow-FFF or F4. This technique can separate and characterize populations such as proteins, colloids, polymers and particulate materials up to about 100 μm in size, preserving their native state and allowing conformational freedom.⁵ The micro-volume variant of FFF, hollow-fiber flow-field flow fractionation (HF5), offers high performance, short analysis time and low dilution, also allowing applications where a disposable device is needed to avoid cross-contamination. Over the FFF separation profile, species differentially forming over time are separated by their hydrodynamic size and can be observed separately; their respective formation can be followed and characterized individually. A combination of studies clearly demonstrated the simultaneous formation of low-density poorly branched polymers (**P**) and dense **NP**. Interestingly, both **P** and **NP** present the most typical feature of melanin-like species, which is the broad absorption band spanning the UV to the near infrared (NIR) region. For this reason, the two species are quite similar in terms of “coloration”, but they can be easily separated and discriminated in real time by FFF, a separation technique that allows one to quantify the contribution of the different morphologies in terms of mass fraction during the PDA formation reaction and hence investigate the formation kinetics of the PDA **P** and PDA **NP**. These results demonstrate that the formation of the **NP** occurs in the first 6 hours of the reaction, while **P** production continues up to 36 hours after the beginning of the reaction. We would like to stress that up to now, no experimental techniques have been proved to be able to separate the different products of DA polymerization in real time. In fact, separation techniques typically exploit a stationary phase that is an obstacle for the analysis of PDA as it is known to “stick” efficiently to every material.^{3a,6} As a consequence, these separative analyses can strongly perturb the PDA system affecting the obtained results and outcome. Since FFF does not use any stationary phase,⁷ it can be efficiently exploited not only for the isolation of the single component of PDA⁸ but also for their analysis from an optical and morphological point of view.⁹

In the second approach, the PDA **NP** was separated from the PDA **P** at the end of the polymerization reaction and were characterized separately by comparing their chemical and physical properties. In particular, the materials were character-

ized by UV-vis absorption spectroscopy, fluorescence spectroscopy, including mapping, Fourier transform infrared spectroscopy (FTIR), dynamic light scattering (DLS), and transmission electron microscopy (TEM). In order to identify and quantify the different functional groups present, pH titration experiments were performed on both the **P** and **NP**. The charges of the species formed at different pH levels were identified by ζ -potential measurements in the case of the **NP** and by gel electrophoresis in the case of the **P**. Our results demonstrate that the **P** and **NP** exhibit very different properties. This is particularly important from the application point of view since the two forms of PDA are expected to offer very different performances in the same application. Here, for example, the antioxidant activities of the **P** and **NP** were compared using the typical DPPH scavenging test showing that the **P** is a much more effective antioxidant than the **NP**. Similar differences are expected when the two forms of PDA are used for other important applications such as surface coating or metal removal. In general, we would like to stress that even the definition of PDA should be reconsidered since this name refers to species with very different chemical, physical, optical and electronic properties.

2. Results and discussion

In this work we investigated the formation of PDA during a typical oxidation process of DA using atmospheric oxygen in a 1 : 3 mixture of EtOH/H₂O in the presence of 0.1 M NH₄OH. This reaction was widely exploited for the production of PDA **NP** with good mono-dispersity and controlled diameter suitable for nanomedicine¹⁰ or for the fabrication of structural pigments.¹¹

As depicted in Fig. 1, the oxidation and polymerization of the molecular precursor DA are known to lead to the formation of **NP**.^{2d,12} However, the formation of a polymeric structure (MW \sim 11.2 kDa) under similar reaction conditions has been also demonstrated by Messersmith and coworkers.¹³ As shown in Fig. 2a, the previously mentioned oxidative-polymerization reaction that leads to the formation of PDA produces a dramatic change, during the reaction, in the color of the reacting solution. In fact, melanin-like materials present a typical broad-band absorption in the red-NIR region responsible for a characteristic dark-brown coloration (while DA only absorbs in the UV region). Hence, the formation of PDA can be simply detected by following, during the reaction, the absorbance of the reaction mixture in the red-NIR region (*e.g.* 700 nm). As shown in Fig. 2a, the absorbance at 700 nm increases during the reaction with a kinetic behavior that could be fitted with a simple first order process with a kinetic constant $k = 0.084 \text{ h}^{-1}$. On the other hand, this change in the absorbance does not allow the identification of the different forms of PDA produced during the reaction process. In order to do this, 5 μL samples of the reaction mixture were injected into the FFF channel at different reaction times and were analyzed using UV-vis absorption and multi angle light scattering (MALS)



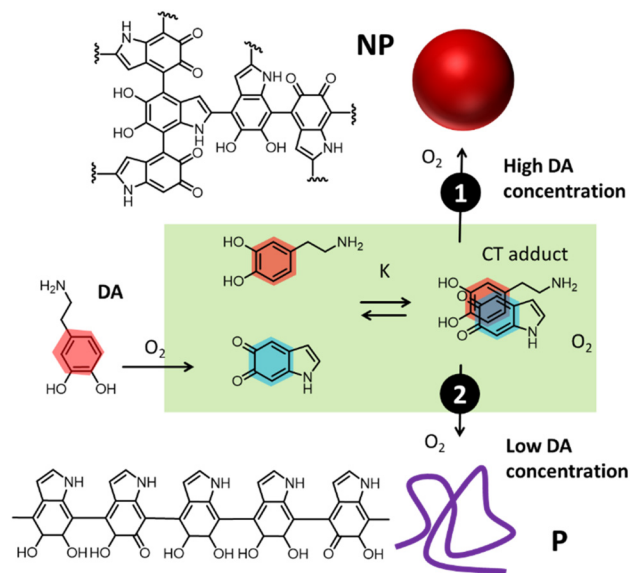


Fig. 1 Oxidation and polymerization of DA occurred through two different pathways leading to the simultaneous formation of NP (path 1) and low-density polymers (P).

detectors. Particularly, the absorbance at 700 nm was followed by the characteristic signal of PDA as mentioned before. As shown in Fig. 2b, FFF made possible the separation of the two different forms of PDA upon elution of the reaction sample. In the exemplificative typical elution plot (fractogram) shown in Fig. 2b (recorded after 4 h reaction), the absorbance is pre-

sented as a function of the elution time and two different absorption peaks can be detected at elution times t_1 and t_2 . Indeed, the presence of these two peaks clearly demonstrates the existence of two different PDA species.

Interestingly, we observed that following the PDA formation reaction for 6 days: (i) the elution profiles always presented the same two peaks with retention times t_1 and t_2 and (ii) the two retention times, t_1 and t_2 , did not change significantly during the reaction. This result can be observed in Fig. 2c where the elution times (t_1 and t_2) are plotted as a function of the reaction time showing that they are almost constant with the values $t_1 = 3.9$ min and $t_2 = 8.4$ min corresponding to peak 1 and peak 2 in the fractogram.

We would like to stress that since the measured retention time is directly proportional to the hydrodynamic radius r_H , we can conclude that beside the complexity of the system, (i) only two main different PDA populations are formed during the reaction, and that (ii) the hydrodynamic radius r_H of these two species does not change during the reaction, being constant at $r_{H1} = 2.7$ and $r_{H2} = 90$ nm.

In order to give complete information about the optical properties of the two species, the 3D spectra at different reaction times are reported in Fig. 3. These spectra represent the absorbance spectra (z-axis) measured in the 200–800 nm range as a function of the absorption wavelength (x-axis) and the retention time (y-axis). In particular, in Fig. 3 we report three representative 3-D spectra acquired at 2 h, 8 h and 6 days of reaction. Both the formed species present the characteristic broad-band absorption ranging from the UV to NIR region, which is typical of melanin-like materials. Moreover, the spectra in

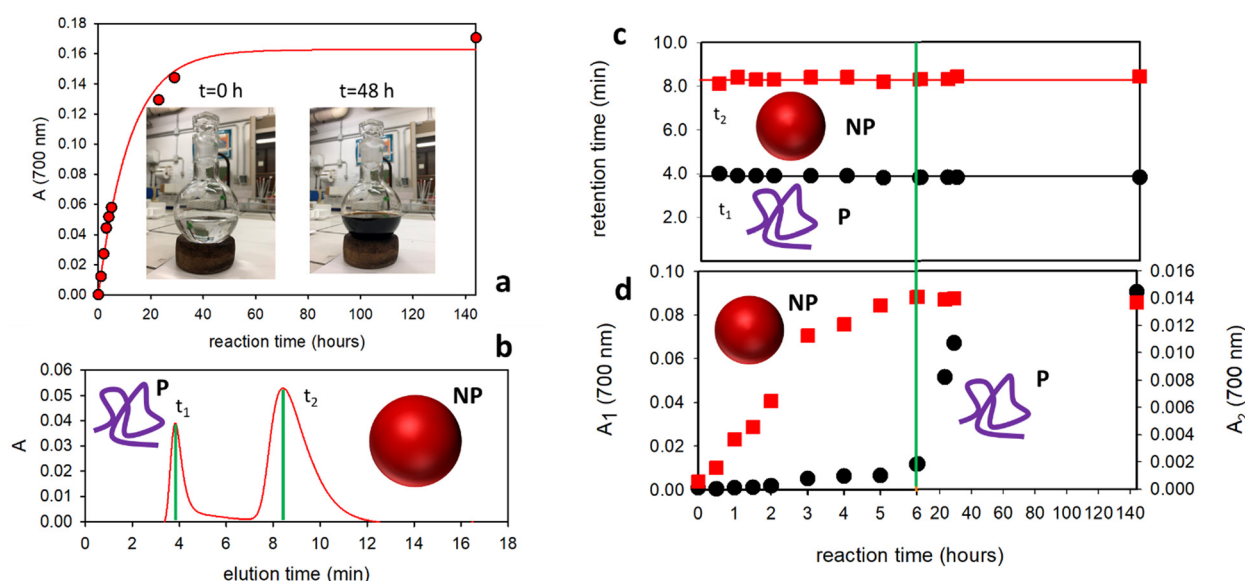


Fig. 2 (a) Absorbance at 700 nm measured for a solution of DA at different times after the preparation (reaction time). The signal could be fitted according to a first-order kinetics with $k = 0.084\text{ h}^{-1}$. (b) A typical fractogram obtained by FFF analysis showing the two peaks at retention times t_1 and t_2 for P and the NP, respectively. (c) Retention times t_1 and t_2 corresponding to the species P (black circles) and NP (red squares) measured at different reaction times by FFF. (d) Absorbance (peak area) of the species P (black circles A_1) and NP (red squares A_2), separated by FFF at different reaction times.



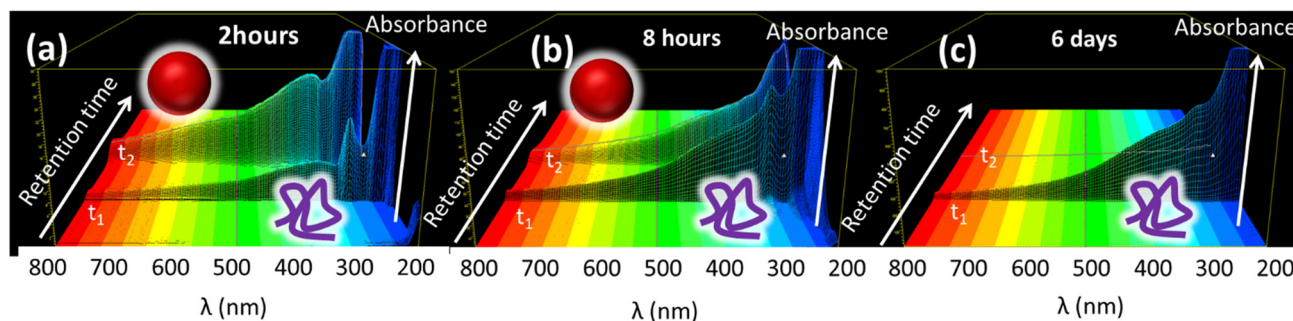


Fig. 3 A 3-D plot acquired for the elution of a solution of DA at different times after the preparation (reaction time). Plots a, b and c correspond to 2 hours, 8 hours and 6 days reaction times, respectively.

Fig. 3 also reveal that while the r_H of the two species does not change during the reaction, in contrast, a relevant difference is observed in the concentration ratio of the two species at different reaction times.

In particular, as shown in Fig. 3a, considering the absorbance in the red-NIR region (typical of melanin-like materials) after 2 h of reaction, the species with a higher retention time t_2 and the largest hydrodynamic radius $r_H = 90$ nm was dominant, while the smaller species with a shorter retention time t_1 and the smallest hydrodynamic radius $r_H = 2.7$ nm produced weaker absorption. As shown in Fig. 3b, after 8 h of reaction, the two species contributed almost equally to the absorption in the NIR region, while after 6 days the smallest species was dominant (Fig. 3c). In order to have complete information about the contribution of the two species to the total absorption in the red-NIR region at different reaction times, the absorbance at 700 nm of peak 1 and peak 2 (A_1 and A_2 , respectively), upon separation by FFF, was reported as a function of the reaction time in Fig. 2d. According to the data shown in this figure, the formation of the species with the largest r_H is dominant during the first hours of the reaction. Moreover, its concentration stopped increasing after about 6 hours and remained unaltered even 6 days after the reaction. In contrast, the concentration of the smaller species increased gradually with time up to about 36 h of reaction.

The results reported above clearly demonstrate that oxidative-polymerization of DA under the analyzed conditions leads to the formation of two different melanin-like species with very different hydrodynamic radii. In order to identify the two species, the reaction was also followed by DLS. The scattering intensity, which depends on both the size of the NP and their concentration, already started increasing 0.5 h after the beginning of the reaction and DLS analysis revealed the presence of the NP of about 60 nm radius. Interestingly, the scattering signal continued increasing up to 6 h of reaction after which it remained at a constant value. This result demonstrates that the scattering signal is associated with the presence of the NP and it stopped changing when their formation was completed. It is also worth noticing that the size of the NP remained unchanged during the whole reaction time and only their concentration changed. The population with the smaller

r_H could not be detected by DLS and the DLS signal did not change significantly after 6 hours of reaction. A combination of FFF with MALS was hence used to analyze the morphology of the smallest species: MALS in fact allows us, in combination with light absorption measurements, to perform morphological analysis and estimate the molecular masses. Different from the case of the NP, morphological analysis of the smallest r_H population demonstrated that it consists of a low-density polymer P with a molecular mass around 100 kDa, which is compatible with the one measured by Messersmith and co-workers. Additionally, a molecular mass of about 10^9 Da was obtained for the population of the NP. We would like to stress that, as shown in Fig. 2c, the retention time of the polymer P, t_1 , did not change during the 140 h reaction time. Since the retention time depends on the size of the polymer we can conclude that this does not change during the reaction.

MALS analysis of the NP, on the other hand, confirms and further verifies the DLS data. After 24 h of reaction, the MALS results revealed a gyration radius $r_G = 71.5 (\pm 2.9\%)$ nm, while the conformational analysis showed a slope of 0.33 corresponding to a spherical conformation. We would like to stress that only in the case of a spherical object the gyration radius r_G is expected to correspond to $0.78 \times r_H$, as in the case of the NP. The formation of the polymer P and the NP was also confirmed by the SEM images shown in Fig. 4.

2.1. Comparison of the properties of the P and NP

As discussed above, the PDA NP was formed only during the first 6 hours of the reaction, while the production of P continued progressively for about 36 hours. The final composition of the dark colored suspension at the end of the reaction, and in particular after 6 days of reaction, was analyzed by separating the NP and P by centrifugation. The final system contained P at a concentration of 3.2 mg ml^{-1} and NP at a concentration of 0.4 mg ml^{-1} .

Despite their similar dark coloration (see Fig. 4a, inset) the P and NP showed very different physical, chemical, optical and electronic properties. As far as optical properties are concerned, the UV-vis spectra recorded for the NP suspension were the combination of an absorption and a scattering contribution that, together, represent attenuation.



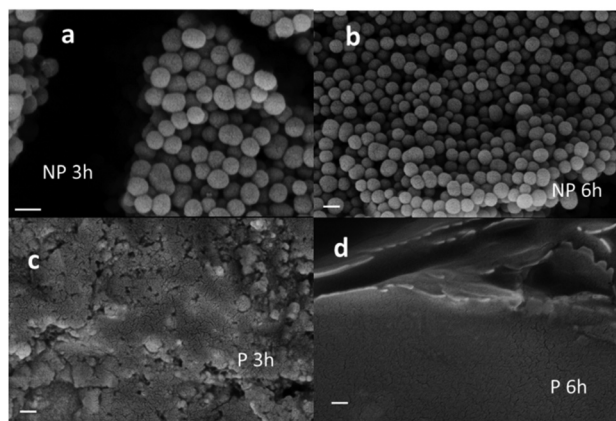


Fig. 4 SEM images of NP obtained after 3 h (a) and 6 h (b) of reaction. SEM images of P obtained after 3 h (c) and 6 h (d) reaction. Scale bar is 200 nm in all the cases.

The mass attenuation coefficient μ_m values for the P and NP are shown in Fig. 5a and they are considerably different, especially at the higher wavelengths. This difference is, to a large extent, due to the different scattering efficiency of the P and NP. Large NP ($d \sim 200$ nm) are in fact expected to scatter light very efficiently. The ability of the P and NP to scatter light differently can be qualitatively observed in the inset of Fig. 5b,

where a laser beam (635 nm) passing through two samples with the same concentration of the P and NP ($5 \mu\text{g mL}^{-1}$) is shown. Only in the case of the NP light is scattered and can be seen at 90° observation. From the quantitative point of view, in order to determine the scattering efficiency of the P and NP, a suspension of SiO_2 NP, which is known to scatter light without absorbing it, was used as a reference. The scattering efficiency as a function of wavelength is reported in Fig. 5b. The scattering spectra confirm that P is very poorly efficient in scattering light, while the NP presents a scattering efficiency that is partially wavelength-dependent and which is as high as 27% around 600 nm. When fluorescence is considered, the P and NP present very different behaviors. In particular, Fig. 5e shows that when the P and NP (same concentration, $10 \mu\text{g mL}^{-1}$) were excited with a light beam at 460 nm, only scattered light with the same color of the excitation could be detected in the case of the NP, while in the case of the P a greenish fluorescence could be detected. These qualitative observations were confirmed using fluorescence steady state spectroscopy. In the case of the NP, the fluorescence spectrum was dominated by the scattering signal, while in the case of the P an excitation-dependent fluorescence was observed. In order to characterize the fluorescence of the P in detail, a fluorescence map of a solution of P ($10 \mu\text{g mL}^{-1}$) was acquired and is shown in Fig. 5c. The fluorescence pattern observable in Fig. 5c is typical of systems with an excitation wavelength-

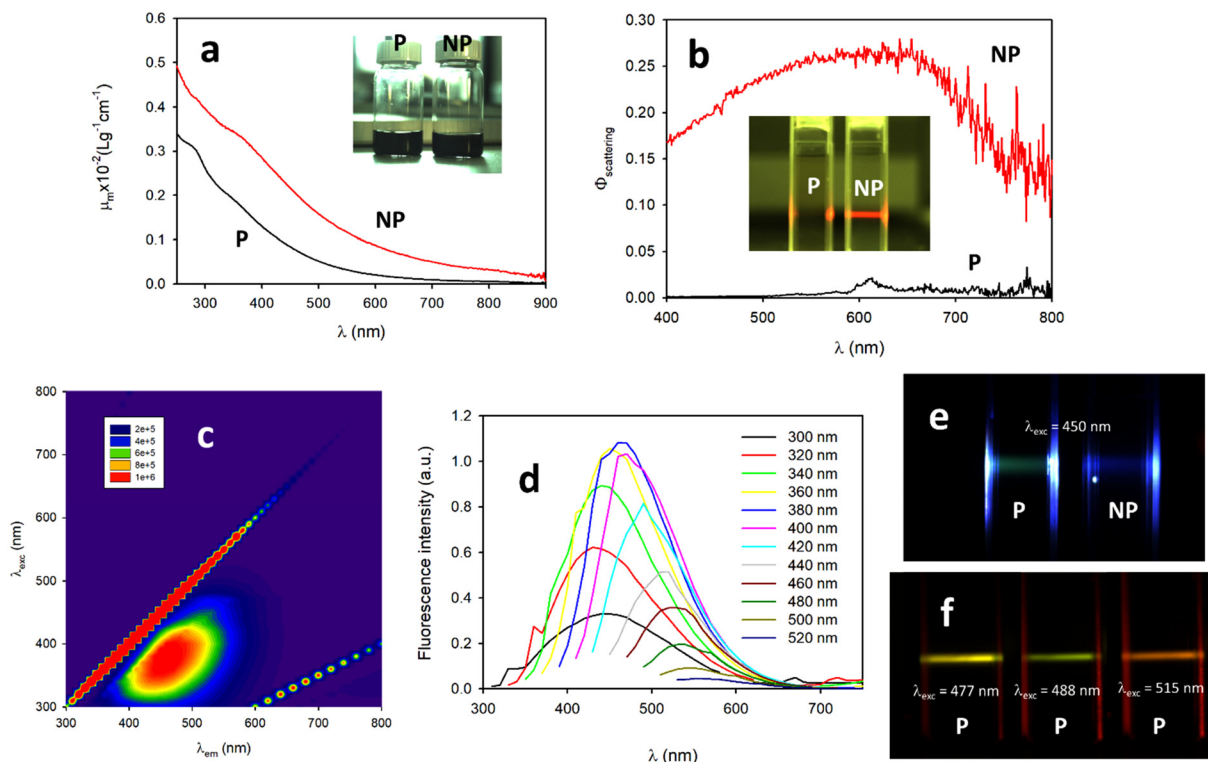


Fig. 5 (a) Mass attenuation coefficients of P and NP; inset: digital picture of P and NP. (b) Scattering efficiency spectrum of P and NP; inset: digital picture of P and NP irradiated with a 635 nm laser. (c) Emission map of P. (d) Fluorescence spectra of P at different excitation wavelengths. (e) Digital picture of P and NP excited with a blue (460 nm) light beam. (f) Digital picture of P excited with different wavelength laser beams.



dependent emission as confirmed by the fluorescence spectra recorded at different excitation wavelengths shown in Fig. 5d.

Different emission colors at different excitation wavelengths for the same **P** sample could also be detected with a digital camera by selecting different wavelengths of an argon laser for the excitation as shown in Fig. 5f. This kind of behavior is typical of systems containing different independent fluorophoric units, which can be independently excited and detected.

In order to better understand the process of the formation of the **P** and **NP** the oxidation of DA was investigated at different initial concentrations of the precursor and the amounts of **P** and **NP** obtained after 36 hours were compared. The results are shown in Fig. 6 and they clearly indicate that

NP are formed only at high concentration of DA while **P** can be formed also at low DA concentration.

2.2. Morphology and functional groups of **P** and **NP**

The different morphologies of the **P** and **NP** were clearly demonstrated by TEM. As shown in Fig. 7a and b, in the case of the **NP**, spherical particles with a diameter of about 160 nm could be detected while, in contrast, upon drying on the TEM grid **P** only a black solid material was formed. The two samples presented two completely different FTIR spectra, as shown in Fig. 7c. Different morphologies are also observed in the SEM images in Fig. 4.

In order to identify and quantify the acidic group present in the **P** and **NP**, pH titration experiments were carried out. For these experiments, solutions of the two species with the same concentration (1 mg mL^{-1}) were used by adding NaOH in order to bring the initial pH to 11. Then, a solution of HCl (1 M) was gradually added and the pH was measured with a pH meter. Fig. 7e shows the pH changes measured upon the addition of HCl in the case of the **P** or **NP** (1 mg mL^{-1}) compared to the changes observed only for a solution of NaOH at pH 11. The results showed that, as expected, for the pure NaOH solution, the pH dropped to a very low value after the addition of 1 mM HCl. In contrast, in the case of the **NP**, the pH drop was shifted by 1 mM , demonstrating the presence of a fraction of a protonable group in the **NP** (2 mmol g^{-1}). Interestingly, in the case of the **P**, the shift of the pH drop was much more consistent than for the **NP**. Additionally, it is possible to identify two different protonation processes, one at about $\text{pH} = 9.0$ and the second one at about $\text{pH} = 6.0$. The

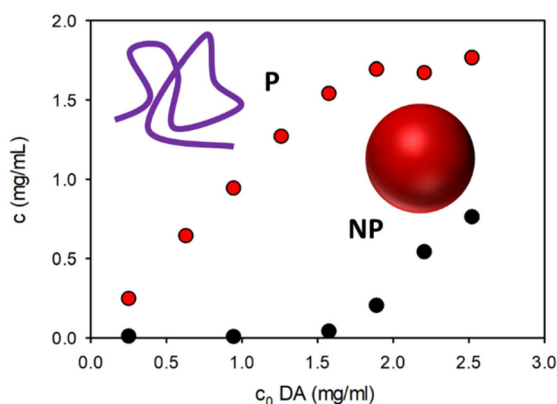


Fig. 6 Concentration of **NP** (black dots) and **P** (red dots) obtained after 36 hours of oxidation of DA at different initial concentrations of DA.

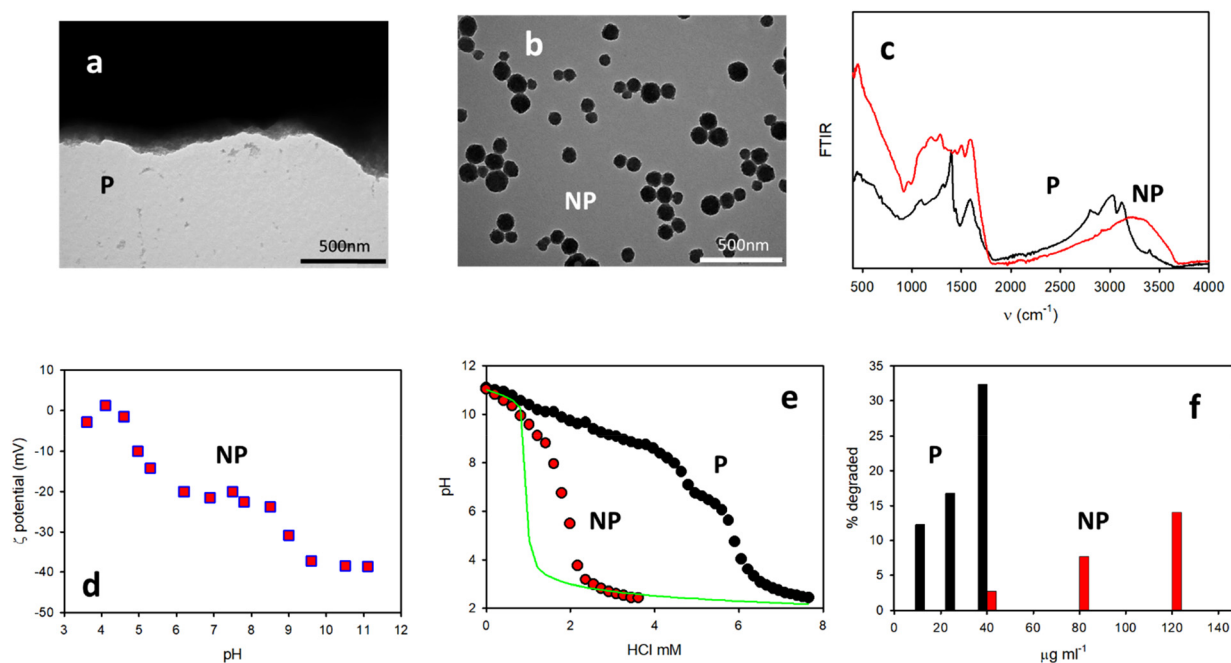


Fig. 7 TEM images of **P** (a) and **NP** (b). (c) FTIR spectra of **P** and **NP**. (d) ζ -potential of **NP** as a function of pH. (e) pH titration of **P** and **NP**. (f) DPPH degraded by **P** and **NP** at different concentrations.



former corresponds to an addition of ~ 4 mM HCl, while the second to an addition of ~ 1 mM HCl. In order to identify the protonable groups present in the **P** and **NP**, we performed further measurements for the determination of the actual charge of the **P** and **NP** as a function of the pH. In the case of the **NP**, this could be done using light scattering to measure the ζ -potential, which is a measurement of the surface charge of the **NP**. These results are shown in Fig. 7d and they clearly demonstrate that the ζ -potential of the **NP** is negative, independent of the pH, and is about 0 mV at pH below 4. This observation demonstrates that, beside the presence of a protonable amino group in the **NP**'s molecular precursor DA, no protonable amines are present in the **NP**. Additionally, based on the data of Fig. 5d, it is possible to state that the **NP** have a strongly negative ζ -potential of ~ 40 mV at an alkaline pH level (11), but a less negative ζ -potential of ~ 20 mV at a neutral pH level (7) and that the protonation occurs at a pH of ~ 9 . Moreover, based on Fig. 5d it is also obvious that further protonation occurred at a pH of ~ 5 leading to a non-charged species. The lack of charges at pH 3 on the **NP** is also demonstrated by the instability of the suspension (colloidal stability is expected to increase with the absolute value of the ζ -potential) that leads to the precipitation of the **NP** after a few hours. All these observations suggest that the protonation at a pH of ~ 9 involves the residual O^- catechol groups, which are still present in the **NP** after DA polymerization. The second protonation at the pH of ~ 5 , on the other hand, is compatible with the presence of carboxylates, COO^- , in the **NP** produced by the oxidation of DA.

In the case of the **P**, the charges at different pH levels could not be determined by light scattering. Hence, agarose gel electrophoresis was performed. In addition, in this case, the results demonstrated that **P** was negative at pH > 3 and it migrated towards the positive electrode in the electrophoretic experiment. At pH < 3 , no migration of **P** could be detected. This observation is consistent with the precipitation of **P**, observed at acidic pH and due to the lack of any charge in this condition mitigating the stability. As discussed above, the results of the titration experiments depicted in Fig. 7e show that the protonation of the **P** takes place at pH levels of about 9 and 6, similar to what was observed for the **NP**. What is radically different on the other hand is the fraction of the OH and COOH groups present in the two species **P** and **NP**. In the case of the **P**, the fraction of OH can in fact be estimated to be as high as 8 mmol g^{-1} and that of COOH to be as high as 2 mmol g^{-1} . In contrast, for the **NP** the total fraction of the OH and COOH groups is about 2 mmol g^{-1} . Moreover, since the two protonation processes observed in the ζ -potential measurements produce a similar change (20 mV), it is expected that the fractions of the OH and COOH groups are similar and hence 1 mmol g^{-1} for both. All these results can be summarized, concluding that in the **NP** the molecular precursor DA undergoes a stronger oxidation and the fraction of the residual OH group is about one order of magnitude less than that in the **P**. This conclusion was demonstrated by experiments on antioxidant activity and, in particular, compar-

ing the DPPH quenching ability of the **P** and **NP**. Briefly, in this kind of experiment the ability of a substance to degrade an easily detectable radical is compared. The results shown in Fig. 7f clearly indicate that at a concentration $40 \mu\text{g ml}^{-1}$, the **P** was able to degrade about 33% of the DPPH radical, while the **NP** degraded only 3%. This result is very interesting since the antioxidant activity of melanin-like materials has been associated with the presence of residual OH catechol groups.¹⁴ Therefore, the decreased antioxidant activity of the **NP** can be ascribed to the low concentration of these groups, which has been demonstrated by the above measurements.

2.3. Mechanism of P and NP formation

Summarizing our results, we demonstrate that: (i) the **NP** presents a high density and hence a high level of cross-linking, while the **P** is less dense and presents a lower molecular weight; (ii) no protonable amines are present neither in the **P** or in the **NP**; (iii) the formation of the **NP** occurs within the first 6 hours of DA polymerization, while the **P** is gradually formed for 36 h; and (iv) the formation of **NP** occurs only at high concentrations of the precursor DA.

We recently demonstrated that the formation of a supramolecular adduct between DA and oxidized DA can be detected during the initial stages of oxidation of DA.⁴ This process favors the reaction of orthoquinone, resulting from DA oxidation, with DA itself leading to the polymerization. Concentration dependent experiments clearly showed that **NP** are formed only at high concentrations of DA and the formation stops when the concentration decreases under a critical value (reached after 6 hours at an initial PA concentration of 2.6 mM). These results suggest that the formation of large aggregates of DA and oxidized DA occurs at high DA concentration leading to the formation of the **NP**.

3. Conclusions

We demonstrated that upon the oxidative-polymerization of DA in the presence of atmospheric oxygen, both dense **NP** and low-density polymer **P** were simultaneously formed. In particular, the **NP** was formed only in the first 6 hours of the reaction, while **P** continued to polymerize up to 36 hours after the beginning of the reaction. The process was driven by the supramolecular association of DA and its orthoquinone product after oxidation, while **P** was formed also at low DA concentration and it resulted mostly from the linear polymerization of the DHI units produced by DA cyclization, the **NP** was formed only at high DA precursor concentration. The **P** and **NP** presented different compositions and optical and chemical properties. In particular, the **NP** is detectable by TEM and SEM as spheres of about 160 nm, a size compatible with FFF, DLS and SLS measurements, while the TEM and SEM images of **P** showed large aggregates. The combination of ζ -potential measurements, gel electrophoresis and pH titration revealed that **P** contained about 8 mmol g^{-1} catecholic OH group and 2 mmol g^{-1} COOH group. In contrast, **NP** contained only a



minor fraction of the catecholic $-OH$ (1 mmol g^{-1}) and less $-COOH$ (1 mmol g^{-1}). The different densities of the catechol units made the **NP** a significantly less effective antioxidant than the **P**.

Regarding their optical properties, both the **P** and **NP** exhibited the characteristic broad band absorption of melanin-like compounds; however, the light attenuation by the **NP** was more effective than that of the **P** especially in the vis-NIR region. Regarding excited state deactivation, the **P** showed an excitation wavelength dependent fluorescence, typical of multi-fluorophoric decoupled systems, while the **NP** presented no fluorescence but they scattered light with an efficiency as high as 27%. The different chemical compositions of the **P** and **NP** was also demonstrated by the very different FTIR spectra. We believe that these results need to be taken into consideration in the design and development of new melanin-based nano-platforms for nanomedicine, energy conversion and environmental remediation.

Author contributions

The manuscript was written through the contributions of all authors. All the authors have given approval to the final version of the manuscript.

Conflicts of interest

There are no conflicts to declare.

Acknowledgements

We acknowledge the Italian Ministry of Education, University and Research (MIUR) (PRIN project: PRIN 2017), 2017E44A9P (BacHound) and PRIN 2020CBEYHC. We acknowledge Dr. Vittorio Morandi and Franco Corticelli (IMM - CNR Bologna) for their contribution in the SEM images present in this paper.

References

- (a) W. Chen, Y. Song, S. Bai, C. He, Z. Guo, Y. Zhu, Z. Zhang and X. Sun, Cloaking Mesoporous Polydopamine with Bacterial Membrane Vesicles to Amplify Local and Systemic Antitumor Immunity, *ACS Nano*, 2023, **17**(8), 7733–7749; (b) L. Liu, R. Li, F. Liu, L. Huang, W. Liu, J. Wang, Z. Wu, N. Reddy, W. Cui and Q. Jiang, Highly Elastic and Strain Sensing Corn Protein Electrospun Fibers for Monitoring of Wound Healing, *ACS Nano*, 2023, **17**(10), 9600–9610; (c) Y. Xing, L. Li, Y. Chen, L. Wang, S. Tang, X. Xie, S. Wang, J. Huang, K. Cai and J. Zhang, Flower-like Nanozyme with Highly Porous Carbon Matrix Induces Robust Oxidative Storm against Drug-Resistant Cancer, *ACS Nano*, 2023, **17**(7), 6731–6744; (d) H. Guo, Z. Cao, J. Li, Z. Fu, S. Lin, L. Wang and J. Liu, Integrating Bacteria with a Ternary Combination of Photosensitizers for Monochromatic Irradiation-Mediated Photoacoustic Imaging-Guided Synergistic Photothermal Therapy, *ACS Nano*, 2023, **17**(5), 5059–5071; (e) M. Song, J. Xing, H. Cai, X. Gao, C. Li, C. Liu, X. Li, X. Fu, S. Ding, W. Cheng and R. Chen, Pomegranate-Bionic Encapsulating Horseradish Peroxidase Using Dopamine Flexible Scaffold-Coated Multishell Porous ZIF-8 To Enhance Immunochromatographic Diagnosis, *ACS Nano*, 2023, 10748–10759; (f) H. Zhao, Z. Liu, Y. Wei, L. Zhang, Z. Wang, J. Ren and X. Qu, NIR-II Light Leveraged Dual Drug Synthesis for Orthotopic Combination Therapy, *ACS Nano*, 2022, **16**(12), 20353–20363; (g) P. Ge, S. Chang, T. Wang, Q. Zhao, G. Wang and B. He, An antioxidant and antibacterial polydopamine-modified thermo-sensitive hydrogel dressing for Staphylococcus aureus-infected wound healing, *Nanoscale*, 2023, **15**(2), 644–656; (h) Y. Zhu, Q. Zeng, Q. Zhang, K. Li, X. Shi, F. Liang and D. Han, Temperature/near-infrared light-responsive conductive hydrogels for controlled drug release and real-time monitoring, *Nanoscale*, 2020, **12**(16), 8679–8686.
- (a) A. Mavridi-Printezi, M. Guernelli, A. Menichetti and M. Montalti, Bio-Applications of Multifunctional Melanin Nanoparticles: From Nanomedicine to Nanocosmetics, *Nanomaterials*, 2020, **10**(11), 2276; (b) A. Mavridi-Printezi, A. Menichetti, M. Guernelli and M. Montalti, The Photophysics and Photochemistry of Melanin-Like Nanomaterials Depend on Morphology and Structure, *Chem. – Eur. J.*, 2021, **27**(66), 16309–16319; (c) J. H. Ryu, P. B. Messersmith and H. Lee, Polydopamine Surface Chemistry: A Decade of Discovery, *ACS Appl. Mater. Interfaces*, 2018, **10**(9), 7523–7540; (d) W. Cao, X. Zhou, N. C. McCallum, Z. Hu, Q. Z. Ni, U. Kapoor, C. M. Heil, K. S. Cay, T. Zand, A. J. Mantanona, A. Jayaraman, A. Dhinojwala, D. D. Deheyn, M. D. Shawkey, M. D. Burkart, J. D. Rinehart and N. C. Gianneschi, Unraveling the Structure and Function of Melanin through Synthesis, *J. Am. Chem. Soc.*, 2021, **143**(7), 2622–2637; (e) H. Liu, Y. Yang, Y. Liu, J. Pan, J. Wang, F. Man, W. Zhang and G. Liu, Melanin-Like Nanomaterials for Advanced Biomedical Applications: A Versatile Platform with Extraordinary Promise, *Adv. Sci.*, 2020, **7**(7), 1903129; (f) Y. Liu, K. Ai and L. Lu, Polydopamine and Its Derivative Materials: Synthesis and Promising Applications in Energy, Environmental, and Biomedical Fields, *Chem. Rev.*, 2014, **114**(9), 5057–5115; (g) F. R. Kohl, C. Grieco and B. Kohler, Ultrafast spectral hole burning reveals the distinct chromophores in eumelanin and their common photoresponse, *Chem. Sci.*, 2020, **11**(5), 1248–1259; (h) C. Grieco, F. R. Kohl, A. T. Hanes and B. Kohler, Probing the heterogeneous structure of eumelanin using ultrafast vibrational fingerprinting, *Nature Communications*, 2020, **11**(1), 4569; (i) T. Li, G. Chen, Z. Xiao, B. Li, H. Zhong, M. Lin, Y. Cai, J. Huang, X. Xie and X. Shuai, Surgical Tumor-Derived Photothermal Nanovaccine for Personalized Cancer Therapy and Prevention, *Nano Lett.*, 2022, **22**(7), 3095–3103;



- (j) S. Ren, X. Tang, L. Liu, F. Meng, X. Yang, N. Li, Z. Zhang, M. Aimaijiang, M. Liu, X. Liu, H. Wang, H. Huangfu, H. Wang, J. Zhang, D. Li and Y. Zhou, Reinforced Blood-Derived Protein Hydrogels Enable Dual-Level Regulation of Bio-Physiochemical Microenvironments for Personalized Bone Regeneration with Remarkable Enhanced Efficacy, *Nano Lett.*, 2022, **22**(10), 3904–3913;
- (k) Y. Huang, L. Mu, X. Zhao, Y. Han and B. Guo, Bacterial Growth-Induced Tobramycin Smart Release Self-Healing Hydrogel for *Pseudomonas aeruginosa*-Infected Burn Wound Healing, *ACS Nano*, 2022, 13022–13036;
- (l) T. Vasileiadis, T. Marchesi D'Alvise, C. M. Saak, M. Pochylski, S. Harvey, C. V. Synatschke, J. Gapinski, G. Fytas, E. H. G. Backus, T. Weil and B. Graczykowski, Fast Light-Driven Motion of Polydopamine Nanomembranes, *Nano Lett.*, 2022, **22**(2), 578–585;
- (m) X. Xu, N. Guillomaitre, K. S. S. Christie, R. K. Bay, N. Bizmark, S. S. Datta, Z. J. Ren and R. D. Priestley, Quick-Release Antifouling Hydrogels for Solar-Driven Water Purification, *ACS Cent. Sci.*, 2022, 177–185;
- (n) Y. Wang, D. Cao, K. Zhang, W. Kang, X. Wang, P. Ma, Y. Wan, D. Cao and D. Sun, Cation-exchange construction of ZnSe/Sb₂Se₃ hollow microspheres coated by nitrogen-doped carbon with enhanced sodium ion storage capability, *Nanoscale*, 2020, **12**(34), 17915–17924;
- (o) M. Fan, Z. Yang, Z. Lin and X. Xiong, Facile synthesis of uniform N-doped carbon-coated TiO₂ hollow spheres with enhanced lithium storage performance, *Nanoscale*, 2021, **13**(4), 2368–2372.
- 3 (a) S. Hong, Y. S. Na, S. Choi, I. T. Song, W. Y. Kim and H. Lee, Non-Covalent Self-Assembly and Covalent Polymerization Co-Contribute to Polydopamine Formation, *Adv. Funct. Mater.*, 2012, **22**(22), 4711–4717; (b) M. D'Ischia, A. Napolitano, V. Ball, C. T. Chen and M. J. Buehler, Polydopamine and eumelanin: From structure-property relationships to a unified tailoring strategy, *Acc. Chem. Res.*, 2014, **47**(12), 3541–3550; (c) X. Zhou, N. C. McCallum, Z. Hu, W. Cao, K. Gnanasekaran, Y. Feng, J. F. Stoddart, Z. Wang and N. C. Gianneschi, Artificial Allomelanin Nanoparticles, *ACS Nano*, 2019, **13**(10), 10980–10990; (d) J. Kong, S. I. Seyed Shahabadi and X. Lu, Integration of inorganic nanostructures with polydopamine-derived carbon: tunable morphologies and versatile applications, *Nanoscale*, 2016, **8**(4), 1770–1788.
- 4 A. Mavridi-Printezi, A. Menichetti, L. Ferrazzano and M. Montalti, Reversible Supramolecular Noncovalent Self-Assembly Determines the Optical Properties and the Formation of Melanin-like Nanoparticles, *J. Phys. Chem. Lett.*, 2022, **13**(42), 9829–9833.
- 5 V. Marassi, M. Mattarozzi, L. Toma, S. Giordani, L. Ronda, B. Roda, A. Zattoni, P. Reschiglian and M. Careri, FFF-based high-throughput sequence shortlisting to support the development of aptamer-based analytical strategies, *Anal. Bioanal. Chem.*, 2022, 5519–5527.
- 6 K.-Y. Ju, M. C. Fischer and W. S. Warren, Understanding the Role of Aggregation in the Broad Absorption Bands of Eumelanin, *ACS Nano*, 2018, **12**(12), 12050–12061.
- 7 (a) A. Zattoni, B. Roda, F. Borghi, V. Marassi and P. Reschiglian, Flow field-flow fractionation for the analysis of nanoparticles used in drug delivery, *J. Pharm. Biomed. Anal.*, 2014, **87**, 53–61; (b) P. Reschiglian, B. Roda, A. Zattoni, M. Tanase, V. Marassi and S. Serani, Hollow-fiber flow field-flow fractionation with multi-angle laser scattering detection for aggregation studies of therapeutic proteins, *Anal. Bioanal. Chem.*, 2014, **406**(6), 1619–1627; (c) V. Marassi, S. Giordani, P. Reschiglian, B. Roda and A. Zattoni, Tracking Heme-Protein Interactions in Healthy and Pathological Human Serum in Native Conditions by Miniaturized FFF-Multidetector, *Appl. Sci.*, 2022, **12**(13), 6762; (d) V. Marassi, D. Calabria, I. Trozzi, A. Zattoni, P. Reschiglian and B. Roda, Comprehensive characterization of gold nanoparticles and their protein conjugates used as a label by hollow fiber flow field flow fractionation with photodiode array and fluorescence detectors and multiangle light scattering, *J. Chromatogr. A*, 2021, **1636**, 461739.
- 8 V. Marassi, S. Casolari, S. Panzavolta, F. Bonvicini, G. A. Gentilomi, S. Giordani, A. Zattoni, P. Reschiglian and B. Roda, Synthesis Monitoring, Characterization and Cleanup of Ag-Polydopamine Nanoparticles Used as Antibacterial Agents with Field-Flow Fractionation, *Antibiotics*, 2022, **11**(3), 358.
- 9 (a) B. Roda, V. Marassi, A. Zattoni, F. Borghi, R. Anand, V. Agostoni, R. Gref, P. Reschiglian and S. Monti, Flow field-flow fractionation and multi-angle light scattering as a powerful tool for the characterization and stability evaluation of drug-loaded metal-organic framework nanoparticles, *Anal. Bioanal. Chem.*, 2018, **410**(21), 5245–5253; (b) V. Marassi, S. Maggio, M. Battistelli, V. Stocchi, A. Zattoni, P. Reschiglian, M. Guescini and B. Roda, An ultracentrifugation – hollow-fiber flow field-flow fractionation orthogonal approach for the purification and mapping of extracellular vesicle subtypes, *J. Chromatogr. A*, 2021, **1638**, 461861.
- 10 Y. Huang, Y. Li, Z. Hu, X. Yue, M. T. Proetto, Y. Jones and N. C. Gianneschi, Mimicking Melanosomes: Polydopamine Nanoparticles as Artificial Microparasols, *ACS Cent. Sci.*, 2017, **3**(6), 564–569.
- 11 M. Xiao, Y. Li, M. C. Allen, D. D. Deheyn, X. Yue, J. Zhao, N. C. Gianneschi, M. D. Shawkey and A. Dhinojwala, Bio-Inspired Structural Colors Produced via Self-Assembly of Synthetic Melanin Nanoparticles, *ACS Nano*, 2015, **9**(5), 5454–5460.
- 12 (a) C. Battistella, N. C. McCallum, K. Gnanasekaran, X. Zhou, V. Caponetti, M. Montalti and N. C. Gianneschi, Mimicking Natural Human Hair Pigmentation with Synthetic Melanin, *ACS Cent. Sci.*, 2020, **6**(7), 1179–1188; (b) Y. Huang, Y. Li, Z. Hu, X. Yue, M. T. Proetto, Y. Jones and N. C. Gianneschi, Mimicking Melanosomes: Polydopamine Nanoparticles as Artificial Microparasols, *ACS Cent. Sci.*, 2017, **3**(6), 564–569; (c) Y. Liu, K. Ai, J. Liu, M. Deng, Y. He and L. Lu, Dopamine-melanin colloidal nanospheres: An efficient near-infrared photothermal



- therapeutic agent for in vivo cancer therapy, *Adv. Mater.*, 2013, **25**(9), 1353–1359.
- 13 (a) P. Delparastan, K. G. Malollari, H. Lee and P. B. Messersmith, Direct Evidence for the Polymeric Nature of Polydopamine, *Angew. Chem., Int. Ed.*, 2019, **58**(4), 1077–1082; (b) K. Lee, M. Park, K. G. Malollari, J. Shin, S. M. Winkler, Y. Zheng, J. H. Park, C. P. Grigoropoulos and P. B. Messersmith, Laser-induced graphitization of polydopamine leads to enhanced mechanical performance while preserving multifunctionality, *Nature Communications*, 2020, **11**(1), 4848; (c) H. Lee, S. M. Dellatore, W. M. Miller and P. B. Messersmith, Mussel-inspired surface chemistry for multifunctional coatings, *Science*, 2007, **318**(5849), 426–430.
- 14 (a) A. Mavridi-Printezi, A. Menichetti, D. Mordini, R. Amorati and M. Montalti, Recent Applications of Melanin-like Nanoparticles as Antioxidant Agents, *Antioxidants*, 2023, 863; (b) Y. Guo, A. Baschieri, F. Mollica, L. Valgimigli, J. Cedrowski, G. Litwinienko and R. Amorati, Hydrogen Atom Transfer from HOO. to ortho-Quinones Explains the Antioxidant Activity of Polydopamine, *Angew. Chem., Int. Ed.*, 2021, **60**(28), 15220–15224.

